

Optical Monitoring of Polypropylene Injection Molding

CHARLES L. THOMAS

*University of Utah
Department of Mechanical Engineering
Salt Lake City, Utah 84112*

and

ANTHONY J. BUR

*National Institute of Standards and Technology
Polymers Division
Gaithersburg, Maryland 20899*

We have constructed an optical fiber sensor for monitoring injection molding and we have developed a model to describe sensor behavior. The sensor consists of a sapphire window at the end of a sleeved ejector pin into which an optical fiber is inserted. The optical view with this sensor is through the thickness of the molded product. The measured optical signal was light that transmitted through the resin, reflected off the back wall of the mold, and retraced its path through the resin to the optical sensor, i.e., light transmitted through twice the thickness of the resin. While monitoring polypropylene during the packing and cooling phase of the molding cycle, we observed a decrease in light intensity due to scattering of light by the growing microcrystals. A characteristic minimum in the transmitted light intensity versus time curve is attributed to scattering by growing crystalline spherulites at the core of the molded product. Cavity pressure was also measured and was found to be an essential parameter in the process model. The model illustrates how temperature, pressure, and crystallinity affect the detected light intensity and clarifies the roles that temperature and pressure play in the crystallization process.

INTRODUCTION

In previous publications we described an optical fiber sensor that occupies the ejector pin channel of a mold using a sleeved ejector pin with a sapphire window at its end (1-5). The view of the molded product with this sensor is through the sapphire window that is positioned flush with the wall of the mold cavity as shown in *Fig. 1*. The molded product was a tensile specimen 16 cm in length by 3.175 mm (1/8 inch) thick. Our previous work demonstrated the use of this sensor to measure fluorescence from a temperature-sensitive dye that was mixed with the processed resin. Both crystallizable and glass forming resins were investigated (1). We found that, although resin solidification can be detected, the interpretation of our data requires a process model that clarifies the roles of temperature, pressure and molecular dynamics during the cooling phase of the process (2, 3, 5). In this paper, we present data obtained during the molding of polypropylene. A fluorescent dye is not involved in the present study. Rather, we consider the optical sensor as a

detector of reflected light only, i.e., light that is transmitted through the resin, reflected off the back wall of the mold, and transmitted back through the resin to the optical sensor. Interpretation of our data is based on a model that incorporates polypropylene crystallization kinetics and attenuation of transmitted light due to scattering by resin crystallites.

EXPERIMENTAL PROCEDURE

The experiments were carried out at Drexel University, Philadelphia, when one of the authors (CLT) was in the Department of Mechanical Engineering at Drexel. The injection molding machine was a BOY 22s Dipronic machine that was interfaced to a personal computer using a data acquisition and control system (6). The personal computer has access to the barrel temperatures and the pressure and flow settings of the machine. The computer was implemented to control pressure and flow settings during the molding cycle and to adjust the holding time and cooling time either on a cycle to cycle basis or immediately in response to sensor feedback. The data ac-

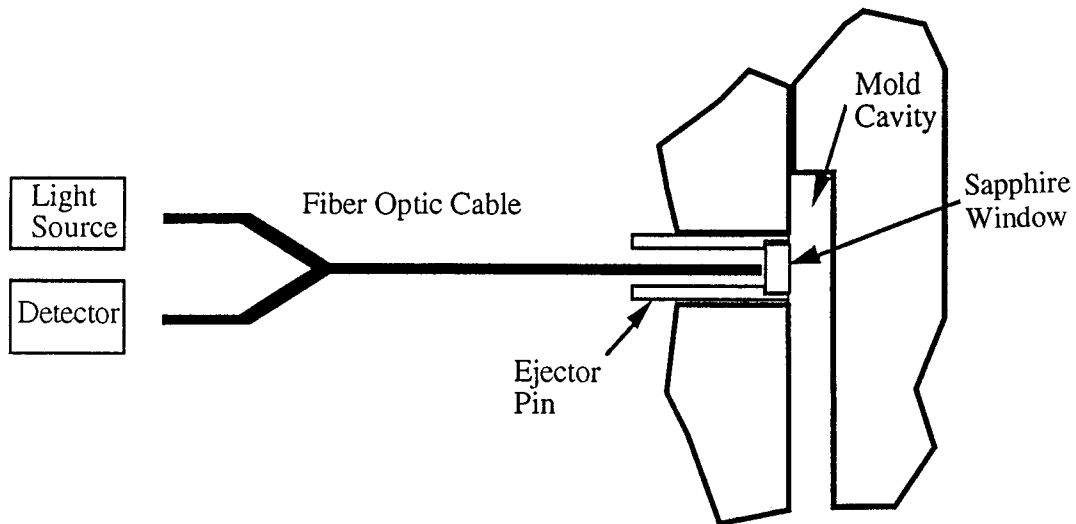


Fig. 1. The optical fiber sensor with its sapphire window flush with the mold cavity wall is shown.

quisition system has analog and digital inputs available for monitoring a series of sensors currently under investigation. The mold cavity is 3.175 mm (1/8 inch) thick and is equipped with optical, pressure and ultrasonics sensors. Results of ultrasonics experiments have been published elsewhere (7-9).

The fiber-optic cable of Fig. 2 consists of a bundle of nineteen 100- μm -diameter fibers, six of which carry light from the source and thirteen of which transmit collected light to the detector. The detector was a silicon photodiode. The light source was a 5 mw HeNe laser that was focused onto the six source optical

fibers. Coupling the laser light to the optical fibers was approximately 30% efficient so that 1.5 mw of the laser power was transmitted to the resin in the mold cavity. Over the one minute duration of the molding cycle time, the intensity of the laser light was stable within $\pm 0.5\%$, and its wavelength, 632.8 nm, was stable within $\pm 0.01\%$. Increased signal sensitivity can be achieved by using a photomultiplier tube detector; also, signal to noise ratio can be improved by using a higher power laser. For these experiments, the silicon photodiode was sufficient because the polypropylene product, with 50% crystallinity, was translucent in

FLUORESCENCE MONITORING OF INJECTION MOLDING

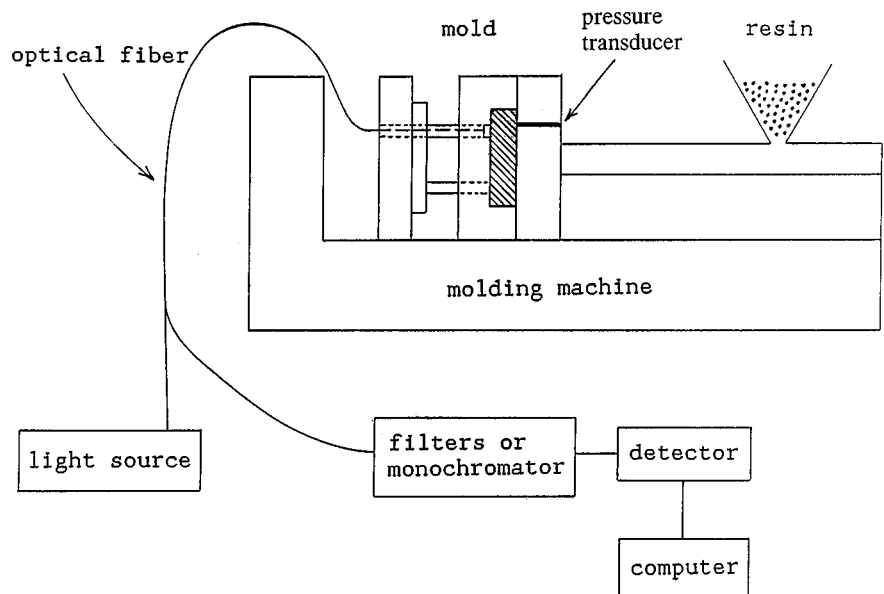


Fig. 2. A schematic of the optical fiber sensor and its light source and data acquisition equipment is shown.

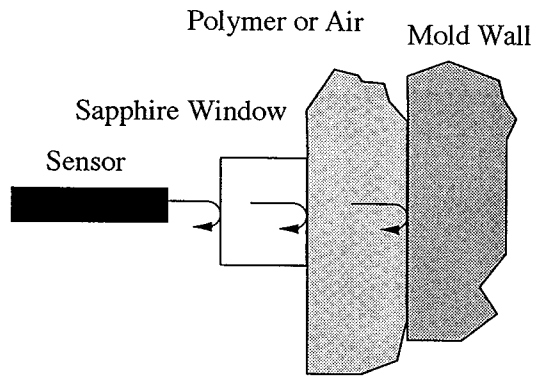


Fig. 3. The light path showing reflections from interfaces is shown.

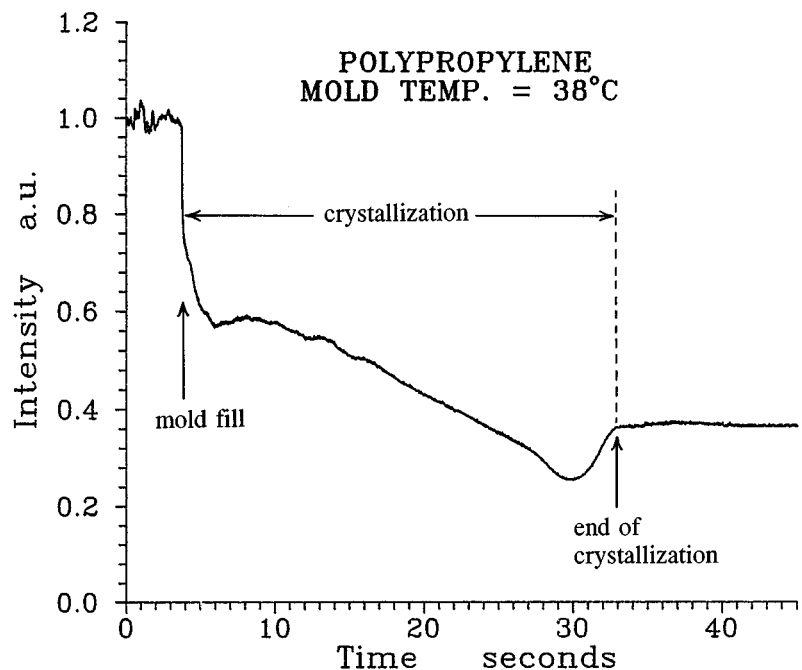
appearance and transmitted approximately 50% of the incident light. The polypropylene resin was Himont PD701 from Montell Polyolefins (6). Resins with higher crystallinity, such as high density polyethylene, are expected to attenuate more light and will probably require a more sensitive detector and more powerful light source arrangement.

Cavity pressure measurements were made using a flush mounted pressure transducer, Dynisco model no. PT449 (6). Pressure measurements have an estimated uncertainty of ± 0.05 MPa. The pressure data were used in the model to calculate the effects of pressure on crystallization kinetics and to calculate compression heating and cooling. Pressure and light intensity signals were acquired and stored in the computer at a rate of 100 Hz.

RESULTS

Figure 3 shows reflections and light paths of the interrogating light beam. The light reflection of interest to us is that which transmits through the resin, reflects off the back surface of the mold, and retraces its path through the resin to the optical sensor. The intensity of this beam is attenuated by microcrystals of polypropylene as they grow and scatter light. This is illustrated in the data of Fig. 4, which are real-time observations of light intensity versus time for molded polypropylene. These data are normalized with respect to the initial intensity value and the estimated uncertainty in the normalized intensity data is ± 0.005 . For the data of Fig. 4, the resin was injected into the mold at 220°C while the mold was held at 38°C by water circulating through coolant channels in the mold. Temperature measurements were made with an estimated uncertainty of $\pm 1^\circ\text{C}$. The time of mold fill was clearly indicated by the abrupt drop in normalized light intensity from 1.0 to 0.78 at $t = 4$ s. This stepwise decrease in intensity is caused by a decrease in reflected light at the front and back interfaces when these interfaces change from sapphire/air to sapphire/resin, and, at the back wall, steel/air to steel/resin. Crystallization proceeded immediately and its effects were observed as a monotonic decrease in normalized light intensity starting at 0.78 and continuing over the time period from 4 to 30 s. The distinct minimum in the curve at 30 s is due to light scattering characteristics of the spherulitic morphology of crystal growth. A final intensity plateau was observed for $t > 33$ s, indicating the end of crystallization. Our model (described below) shows that the minimum at $t = 30$ s coincided with crystallization at the core of the resin product. From the shape of the curve at the minimum, we estimate

Fig. 4. Real-time measurement of light intensity versus time is shown for injection molding of polypropylene for mold temperature at 38°C .



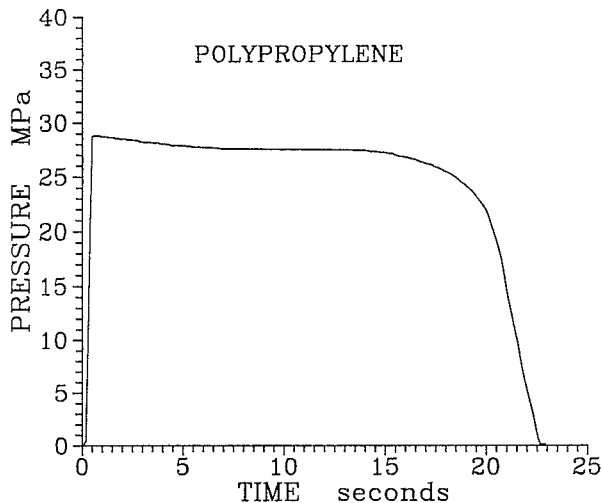


Fig. 5. Cavity pressure is plotted versus time for injection molding of polypropylene.

that the duration of core crystallization was 6 s. Cavity pressure measurements corresponding to the intensity data of Fig. 4 are shown in Fig. 5.

In order to demonstrate that the observed light was light reflected from the opposite wall of the mold, we carried out a control experiment for which the reflecting mold wall was blackened with a light absorbing paint so that reflection from the wall was near zero. The data are shown in Fig. 6, where we present a side-by-side comparison of results from the blackened and non-blackened cases. It is seen that, after mold filling occurred at $t = 8$ s, the detected light from the blackened mold remained constant while resin crystallization was underway. These data show that the observed intensity of Fig. 4 was light that reflected from the back wall and that none of the detected light was back scattering from the resin crystals. Our interpre-

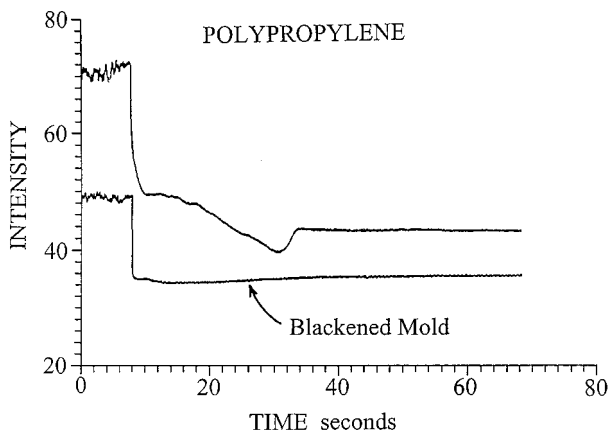


Fig. 6. The results of the control experiment with blackened mold surface are shown.

tation of the data and the model construction will focus on the attenuation of light that traversed twice the thickness of the molded product.

In Fig. 7, we show the effect of changing the temperature of the mold. With increasing mold temperature, the intensity minimum moves to longer times indicating that the crystallization process takes longer for the higher mold temperatures. The distinctive minimum is a universal observation, present in all curves, and is due to scattering from growing spherulites, a phenomenon we discuss in more detail below. We also observe in Fig. 7 that the final plateau of intensity is highest for the mold of lowest temperature. The final plateau is assumed to be inversely proportional to crystallinity, and, from these observations we would conclude that the higher mold temperature causes slower crystallization and higher crystallinity. This is borne out by the data of Fig. 8 where we have plotted crystallinity versus plateau intensity. Here, the crystallinity was calculated from density measurements and has an estimated uncertainty of ± 0.005 (10)

DISCUSSION

Two sources of light scattering cause the decrease in light transmission: (a) the growing spherulites, which are the basic morphological structures of the crystalline phase, and (b) the microcrystals within the spherulites. The distinctive minimum in the intensity data at $t = 30$ s (Fig. 4) is attributed to light scattering by polymer spherulites which was first observed by Stein and coworkers (11, 12). The spherulitic light scattering is caused by the difference in index of refraction between the amorphous phase and the crystalline spherulite. A qualitative illustration of the effect is shown in Fig. 9, where we show growing crystalline spherulites with index of refraction n_2 in a matrix of amorphous resin with index of refraction n_1 . The Stein model yields an attenuation coefficient α_s that has quadratic dependence on the volume fraction of spherulites ϕ ,

$$\alpha_s = A(\phi - \phi^2) \quad (1)$$

where A is an amplitude factor (11, 12). $\alpha_s = 0$ for two cases, $\phi = 0$, no crystallinity, and $\phi = 1$, the end of crystallization, and between these extremes α_s assumes a maximum when $\phi = 0.5$. When crystallization is complete, the spherulites are entirely volume filling ($\phi = 1$) and there is no surrounding amorphous material to offer a differential of index of refraction; therefore, $\alpha_s = 0$ for this condition. Microscopic examination of microtomed specimens of the molded product showed large spherulites at the core, 20 to 50 μm in diameter, and smaller spherulites near the skin. At the skin, some spherulites were distorted in shape, presumably because of shearing effects during mold filling. There was no evidence of transcrystallization at the skin. The smaller spherulites at the skin populated a region that was 100 to 200 μm in depth. The larger spherulites occupied the remainder of the volume.

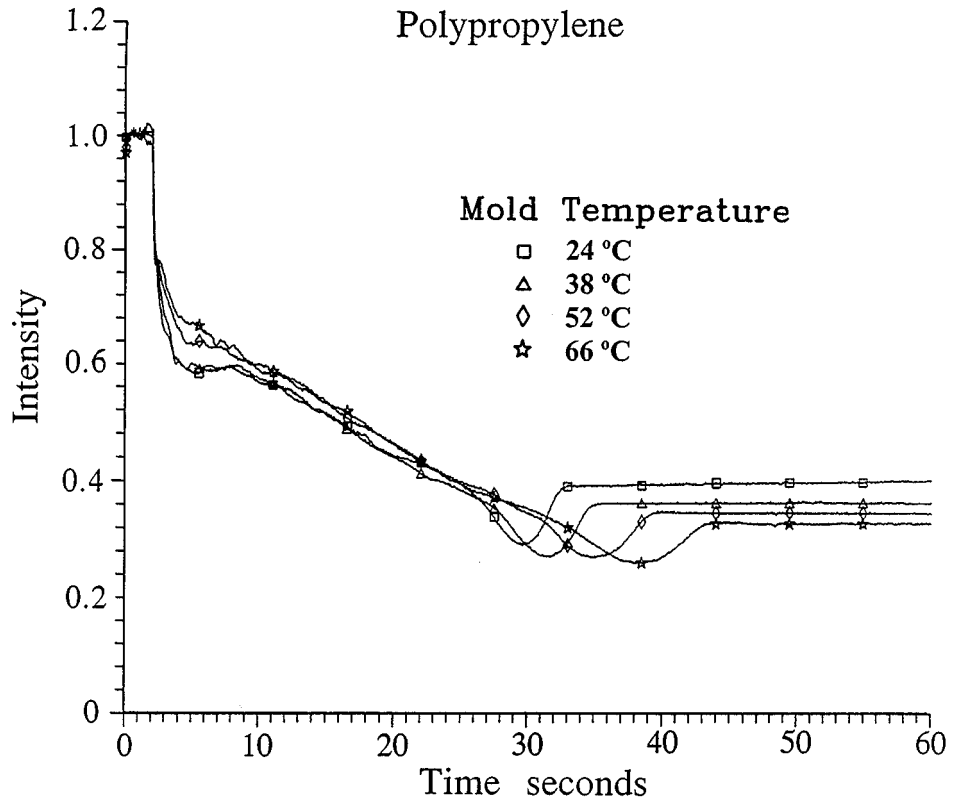


Fig. 7. Real-time measurement of light intensity versus time is shown for injection molding of polypropylene for mold temperatures at 24°C, 38°C, 52°C, and 66°C.

The second source of light scattering, microcrystals within the spherulites, is due to the fact that each spherulite of polypropylene is approximately 50% crystalline, containing a mix of microcrystals and amorphous material. This scattering results in attenuated light transmission. It is seen in Fig. 4 that the

final value of transmitted light (0.36) is approximately half the initial value (0.78). In the model calculation, we will assume that the attenuation of light traversing a distance x in the resin follows an exponential decay function, $e^{-\beta x}$, where the attenuation coefficient β is a linear function of crystallinity χ , $\beta = C\chi(x) \text{ cm}^{-1}$. C is a

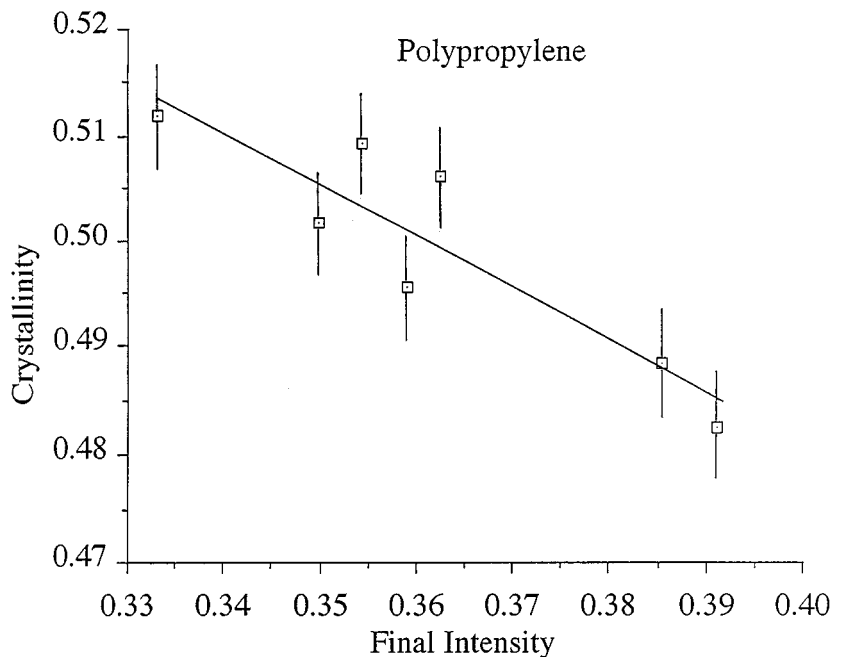
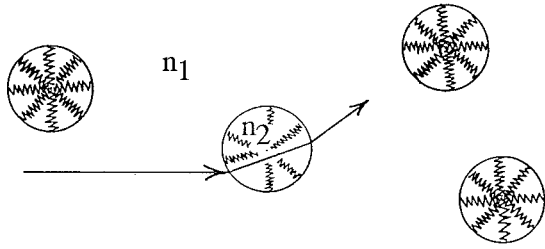


Fig. 8. Crystallinity is plotted versus final light intensity. The error bar on each datum point is the estimated uncertainty of the crystallinity measurement.

STEIN LIGHT SCATTERING



$$I_{scatt} = A(\phi - \phi^2)$$

ϕ = volume fraction of spherulites

$\phi = 0$ at beginning of crystallization: $I_{scatt} = 0$
 $\phi = 1$ at end of crystallization: $I_{scatt} = 0$

Fig. 9. A schematic of the Stein light scattering process is shown. Here, n_1 and n_2 are the indexes of refraction for the amorphous and crystalline phases respectively, ϕ is the volume fraction of spherulites and I_{scatt} is the scattered light intensity.

constant of proportionality. We note that, during the process of resin cooling and crystallization, χ will be a function of position.

Model Calculations

The objectives of the model analysis are to calculate light intensity as a function of time and to examine those factors that contribute to the observed light intensity profiles. The model consists of two modules that are illustrated in Fig. 10. First, the thermal diffusion equation is solved by the method of finite element differences yielding temperature and crystallinity arrays as a function of position and time. Second, crystallinity arrays are used to calculate the transmitted light intensity as a function of time. These calculations were carried out using a one-dimensional finite element mesh of 82 elements, which defines the resin thickness. Details of the finite element difference calculation are presented in the Appendix.

The thermal diffusion equation, including terms for compression and the heat of crystallization, is

$$\rho C_p \frac{\partial T}{\partial t} = \Delta(k\Delta T) + \dot{q}_a + \dot{q}_c \quad (2)$$

where C_p is specific heat, ρ is density, k is thermal conductivity, \dot{q}_c and \dot{q}_a are rates of heat generation by crystallization and by compression heating or cooling. C_p and k values and their temperature dependencies for polypropylene were obtained from Van Krevelen (13), Wunderlich (14), and Kamal (15).

\dot{q}_a is created in the process by the application and release of packing pressure. In an adiabatic process, the temperature change ΔT associated with a change

MODEL CALCULATION FOR TRANSMITTED LIGHT

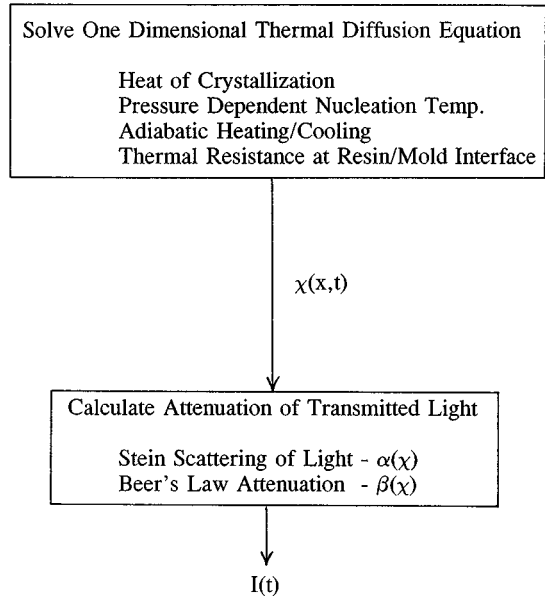


Fig. 10. The modules of the model calculation are shown.

of applied pressure ΔP at constant entropy is given by

$$\Delta T = \frac{Tv\alpha}{C_p} \Delta P \quad (3)$$

where v is specific volume and α is the coefficient of volume thermal expansion (16). \dot{q}_a is calculated from

$$\dot{q}_a = \rho C_p \dot{T} = T\alpha \dot{P} \quad (4)$$

We calculate α for each specific volume, which, for a crystalline compound, is

$$v = \chi v_c + (1 - \chi) v_a \quad (5)$$

where v_a and v_c are amorphous and crystalline specific volumes. $\alpha = (1/v)(dv/dT)$ is obtained from Eq 5 using the Hartmann-Haque equation of state for v_a (17), specific volume measurements of Zoller (18), and data from Wunderlich (14). The Hartmann-Haque equation is given as

$$(P/B_0)(v_a/V_0)^5 = (T/T_0)^{3/2} - \ln(v_a/V_0) \quad (6)$$

where $V_0 = 1.0870 \text{ cm}^3/\text{g}$, $B_0 = 2050 \text{ MPa}$, and $T_0 = 1394 \text{ K}$ for polypropylene (17). Equations 5 and 6 are combined with values of v_c and dv_c/dT from the cited literature to calculate α , which is then used in Eq 4 to obtain \dot{q}_a .

The heat of crystallization \dot{q}_c is given by

$$\dot{q}_c = \rho H_f \dot{\chi} \quad (7)$$

where H_f , the heat of fusion, is 200 J/g for polypropylene (14). The rate of crystallization $\dot{\chi}$ is obtained from the Avrami equation,

$$\chi = 1 - e^{-Kt^3} \quad (8)$$

where K is the Avrami rate constant. Thus,

$$\frac{d\chi}{dt} = (1 - \chi)[3K(-K^{-1}\ln(1 - \chi))^{\frac{2}{3}} + (-K^{-1}\ln(1 - \chi))\frac{dK}{dt}] \quad (9)$$

where we have used Eq 8 to eliminate t . For the model calculation, dK/dt is replaced with $(dK/dT)(dT/dt)$, and dT/dt is obtained from the change in temperature that occurs during the time step dt between successive finite difference calculations of Eq 2. K for spherulitic crystal growth is given as

$$K = \frac{4\pi}{3} Nu^3 \quad (10)$$

where N is the number of spherulites per cm^3 . u is the radial velocity of the sphere, which is expressed as

$$u = u_0 e^{-\frac{E_a}{RT}} e^{-\frac{W}{kT}} e^{\gamma_p P} \quad (11)$$

where E_a is the activation energy for diffusive transport of a polymer chain at the crystal/amorphous interface, W is the crystal surface nucleation work factor, and P is pressure. γ_p is the pressure shift factor, which accounts for the increase in rate of crystal growth under applied pressure (18, 19). The characteristic crystallization time increases by a factor of 5 to 10 under the pressure applied during injection molding, 28 MPa (see Fig. 5) (19). The increased rate can be accounted for by setting γ_p equal to 0.065 MPa^{-1} .

E_a and W were obtained from Mandelkern *et al.* (20). Although E_a is often calculated from the WLF equation by others (21), we found that an activation energy close to Mandelkern's value yielded a better fit to the data. We used $E_a = 46 \text{ kJ/mole}$ for our calculations. W is expressed as

$$W = \frac{\Delta H T_m}{RT_c(T_m - T_c)} \quad (12)$$

where ΔH is an activation energy, T_c is the crystallization temperature, and the melting temperature T_m is 165°C at atmospheric pressure but shifts with pressure according to $T_m = 165 + 0.4P(\text{MPa})$ °C (14, 22). Mandelkern *et al.* found that the ratio $\Delta H/R$ is 263 °K (20). Values of u_0 and N were taken from Van Krevelen and were assigned values 10^5 cm/s and 10^6 cm^{-3} (13). Equations 10 and 11 express the temperature dependence of K from which the value of dK/dT is obtained. The product $(dK/dT)(dT/dt)$ is then substituted in Eq 9, yielding a value of $d\chi/dt$.

The Avrami equation describes crystal growth after the nucleation has occurred. For the model, it is essential that we establish the time of the nucleation event that is dependent on the magnitude of supercooling. At atmospheric pressure under conditions of

rapid cooling, we observed nucleation occurring at 110°C. Application of pressure increases the melting temperature, thereby increasing supercooling. In order to simulate the supercooling increase with pressure, the program code contained a statement that $\dot{\chi} = 0$ if $T > 110(\text{°C}) + 0.4P(\text{MPa})$ (14, 22).

The assumed boundary conditions were that the extreme outer edge of the mold (steel/air interface) was an insulating boundary. Because of symmetry of the mold, the midpoint of the resin thickness is an insulating boundary; in addition, the temperature profile in the resin should be symmetric about the midpoint resulting in $dT/dx = 0$ at that point. Another boundary we need to consider is the interface between resin and mold where a thermal resistance is established, impeding the transport of heat from the resin. Here, we rely on work by Kamal and coworkers (15), who measured the thermal flux at this interface and calculated a thermal transport coefficient h for the boundary. h was found to have time dependence that could be approximated by exponential decay

$$h = h_0 e^{-t/\tau} + h_\infty \quad (12)$$

where $h_0 = 5h_\infty$. In the model calculation, h_∞ is used as a fitting parameter, and $\tau = 0.3 \text{ s}$ is a value obtained from Kamal (15). A boundary condition at the resin/mold interface is that the heat flux is continuous.

Equations 3 through 11 in conjunction with the boundary conditions and the pressure data of Fig. 5 were employed in the solution of Eq 2 to obtain both temperature and crystallinity arrays as a function of position and time. A finite difference calculation was carried out using time steps of 1 ms starting with initial conditions: resin temperature at 220°C and a steel mold temperature at 38°C. The finite element mesh consisted of 82 elements across the thickness of the resin (3.1875 mm) and 10 elements across the steel mold wall (2.54 cm). The calculation was started by explicitly calculating the heat flux into the steel mold from the resin element nearest the steel wall during 1 ms. Details regarding the model calculation are contained in the Appendix.

The calculated results are shown in Figs. 11 through 15. In the case of the calculated temperature/time profile, Fig. 11, the data are shown for five equi-spaced positions in the resin from the skin (the resin/mold interface) to the inner core. The effects of compression heating and the heat of crystallization are readily seen. Initially, the skin temperature falls rapidly followed by a small increase (at $t = 3 \text{ s}$) due to heat of crystallization and to a decrease in the value of h .

The core temperature initially increases (compression heating) and then decreases to a plateau value at 130°C before rising again at 25 s. Fluctuations in temperature are readily seen at the skin and at positions 25%, 50% and 75% into the core. These fluctuations are due to local heating and cooling cycles that accompany crystallization. When a sector crystallizes, it generates heat, which, if it is not carried away quickly enough, will raise the local temperature. A rise in tem-

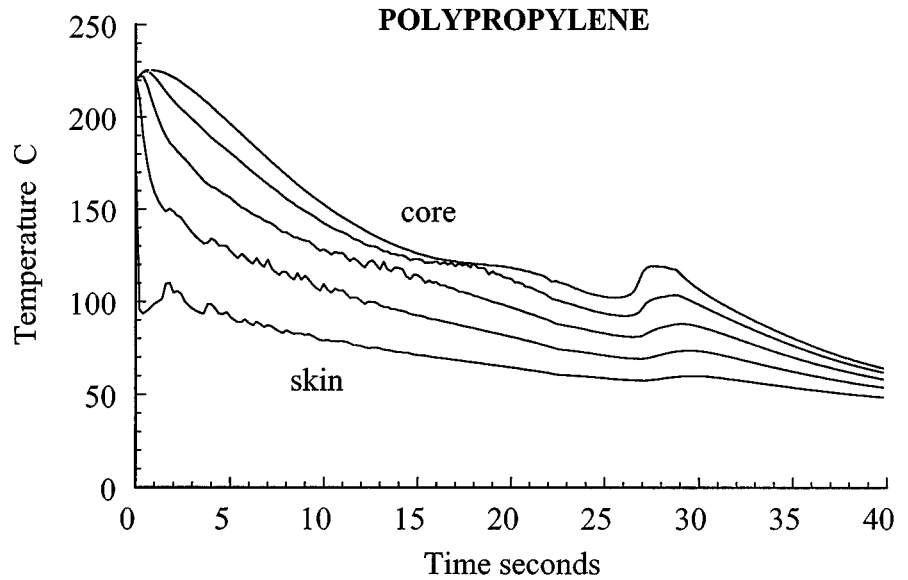


Fig. 11. Calculated temperature versus time profiles are shown for five positions equi-distanced from skin to core. The calculations were made for transport coefficient $h_c = 0.045 \text{ J}/(\text{cm}^2 \text{ s}^\circ\text{C})$.

perature causes a slower rate of crystallization and a lower rate of heat generated by crystallization permitting the sector to cool as heat is conducted away. A cooler local temperature increases in the rate of crystallization and the rate of heat generation with the result that temperature increases again. The cycle continues, producing up and down temperature fluctuations until local crystallization is complete. As crystallization proceeds from skin to core (Fig. 13), we see that temperature fluctuations of Fig. 11 die out soon after the crystallization front has passed, i.e. at 9, 13, 16 and 19 s for the skin, 25%, 50% and 75% layers.

The curve corresponding to the 75% layer assumes a temperature plateau (130°C) at 15 s because heat of crystallization generated by crystallizing resin at positions closer to the skin impedes the transport of heat

from that sector. As the crystallization front reaches the core at $t > 24 \text{ s}$, its temperature increases by a substantial amount, 15°C, due to heat of crystallization. This large temperature excursion, which is not seen at other positions, is due to the fact that the center position of the core is an insulating boundary so that heat generated there can diffuse in one direction only. Except for the core, crystallization occurs at elevated pressures, approximately 28 MPa. By the time the core is crystallizing the pressure has dropped to atmospheric with the consequence that core crystallization is significantly slower than that of the rest of the molded product. The higher temperature at the core also slows crystallization, and creates a condition under which the Stein light scattering effect is distinctly expressed in the light transmission curve.

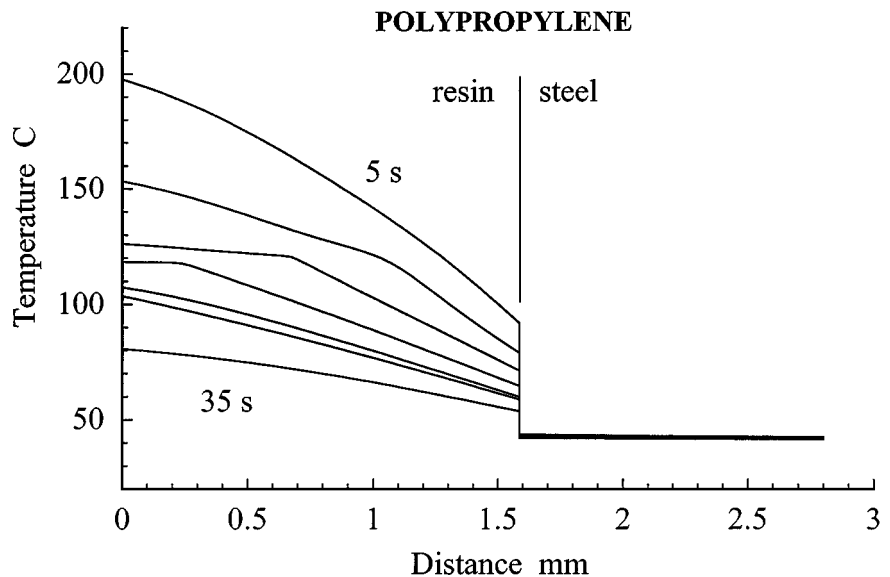


Fig. 12. Calculated temperature versus distance profiles in both the resin and the steel mold are shown for selected times. The calculations were made for transport coefficient $h_c = 0.045 \text{ J}/(\text{cm}^2 \text{ s}^\circ\text{C})$.

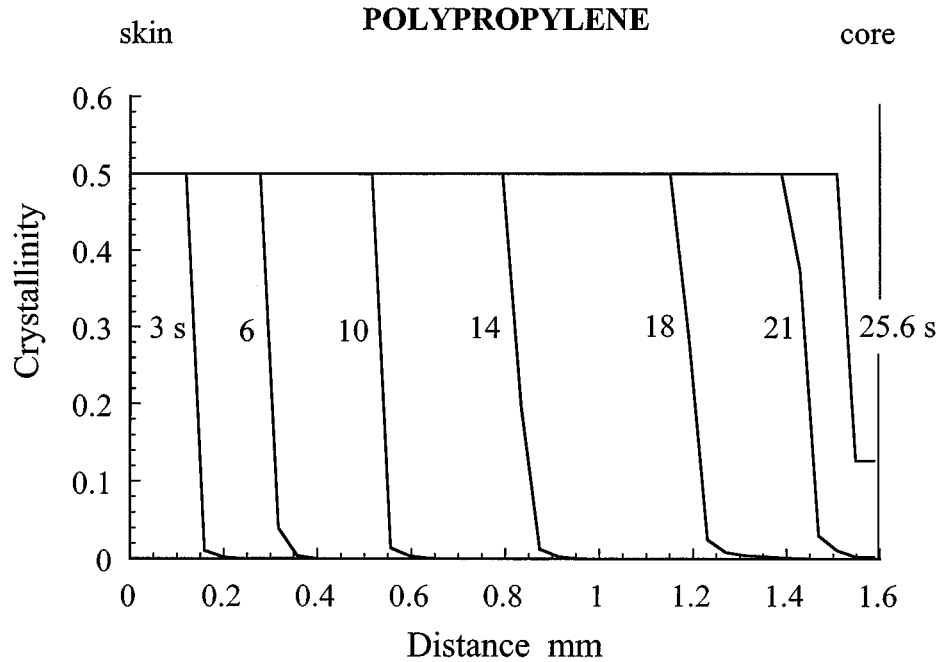


Fig. 13. Calculated crystallinity is plotted versus distance for the indicated times. The calculations were made for thermal transport coefficient $h_c = 0.045 \text{ J}/(\text{cm}^2 \text{ s } ^\circ\text{C})$.

Another view of the calculated temperature results is shown in Fig. 12 where we plot temperature/position profiles in both resin and the steel mold. The temperature step at the resin/steel interface is due to the presence of the thermal resistance at this interface. A finite temperature step remains in place in order to maintain a continuous heat flux across this boundary. The maximum change in the calculated average temperature of the steel mold is 3°C during the process and cannot be seen on the scale of Fig. 12.

Calculated crystallinity versus distance profiles in the resin at selected times, Fig. 13, show a crystalline

front proceeding into the molded resin from skin to core. The calculation yielded complete crystallization at $t = 29.3 \text{ s}$ for a mold temperature of 38°C . From the shape of the curve at the minimum of our real-time observation, Fig. 4, we estimate that the duration of core crystallization was 6 s. Referring to the calculated results of Fig. 13, the final 6 seconds translates to an estimated core width of $150 \mu\text{m}$. Using this core width and the magnitude of the minimum observed in the data of Fig. 4, we calculate $A = 45 \text{ cm}^{-1}$ (Eq 2) by assuming that the minimum occurred when $\phi = 0.5$.

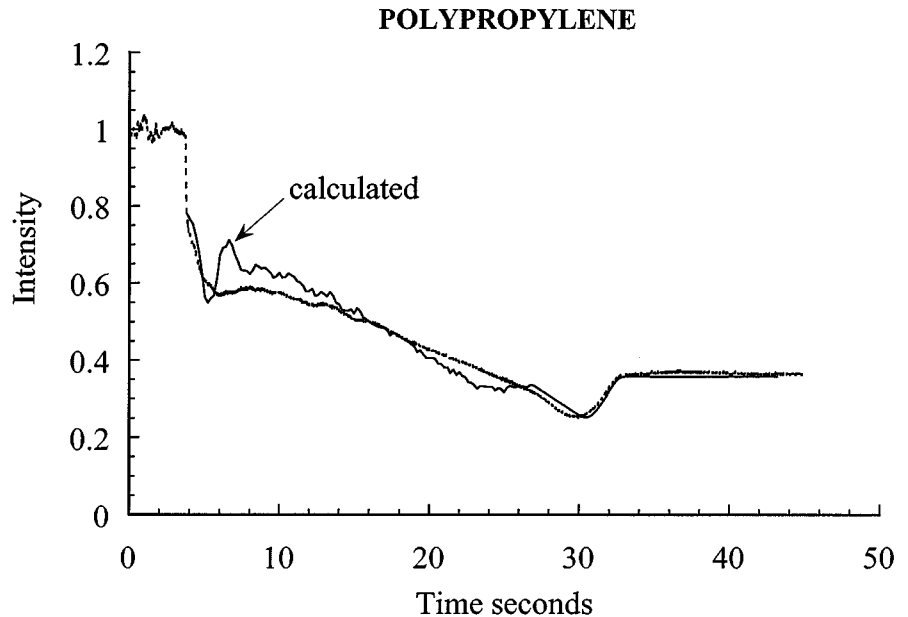


Fig. 14. Calculated and observed light transmission intensities are plotted versus time. The calculations were made for thermal transport coefficient $h_c = 0.045 \text{ J}/(\text{cm}^2 \text{ s } ^\circ\text{C})$.

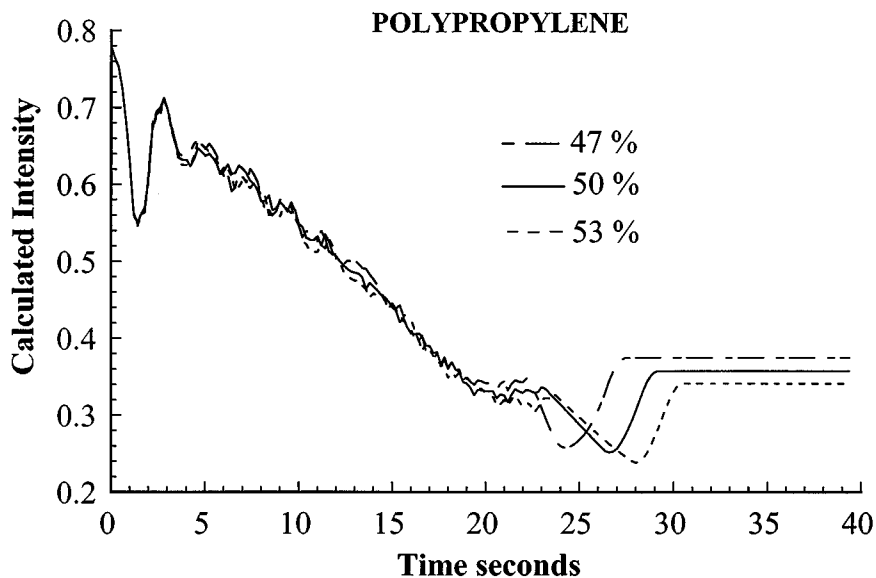


Fig. 15. Calculated light intensity is plotted versus time for final crystallinities of 47%, 50%, and 53%. The calculations were made for thermal transport coefficient $h_{\infty} = 0.045 \text{ J}/(\text{cm}^2 \text{ s } ^\circ\text{C})$.

Having obtained crystallinity arrays, we proceed to the second part of the model and calculate transmitted light intensity, taking into account the attenuation of light transmission due to scattering by spherulites and scattering caused by the microcrystals within the spherulites. As described above, scattering by spherulites obeys the Stein scattering law, Eq 1, and scattering by microcrystals causes exponential decay in transmitted light. The transmitted light I_t can be expressed as

$$I_t = I_0 e^{-\int_0^d [2\alpha_s(x) + 2\beta(x)] dx} \quad (13)$$

where I_0 is the incident light, and the factor 2 in the exponent indicates that the light has traversed twice the thickness. α_s is obtained from Eq 1, and $\beta = C\chi \text{ cm}^{-1}$, where C is a constant. It is assumed that the crystallinity of the spherulites is 50% at all times, i.e. $\chi = 0.5\phi$. At $t = 0$, the bracketed term of Eq 13, [...], is equal to 0 because $\chi = 0$. Thus, at $t = 0$, $I_t = I_0 = 0.78$ which is the initial value of the observed light transmission on the normalized scale of Fig. 4.

Two adjustable parameters were used to calculate the light intensity shown in Fig. 14. The thermal transport coefficient h was adjusted so that the end of crystallization occurred at 33 s, yielding a value $h_{\infty} = 0.045 \text{ J}/(\text{cm}^2 \cdot \text{s} \cdot \text{g})$. C was adjusted so that the amplitude of the transmitted light at long times ($t > 33 \text{ s}$) agreed with the observation. $C = 1.2 \text{ cm}^{-1}$ was found to give the closest agreement with the measurement. By fixing I_0 at 0.78 and C at 1.2 cm^{-1} , we force the calculated curve to be in agreement with observed data at $t = 4 \text{ s}$ and $t = 33 \text{ s}$ (Fig. 14 time scale). The quality of the fit to the observed data is judged by the shape of the curve between these two times.

The calculated curve, Fig. 14, clearly shows the distinct Stein scattering minimum and shows that this effect is described by a quadratic scattering

function. It is interesting that the full Stein scattering curve was not seen until the very last elements at the core were crystallizing, even though the Stein function is operative throughout the calculation from skin to core. This is because of overlapping scattering effects from neighboring elements and because the rate of crystallization is relatively rapid for crystallization at elevated pressures. As the crystalline front moves through the sample (Fig. 13), sectors near the front are in various stages of crystallization, some at the beginning for which $\alpha_s \approx 0$, some in the middle for which $\alpha_s = A/4$, and some near the end for which $\alpha_s \approx 0$. Overlapping scattering from the different elements washes out the distinct quadratic profile and results in an average attenuation. It is only when the last elements are crystallizing, for which crystallization is slow and there are no other competing crystallizing sectors, that we see the full Stein function expressed. Both the calculated and measured curves (Fig. 14) display minor minima and wiggles, particularly at $t = 5$ to 6 s , all of which are due to Stein scattering but do not exhibit the full Stein curve because of overlapping scattering from neighboring regions.

The primary discrepancy between calculated and observed values occurs when the skin crystallizes at $t \approx 6 \text{ s}$. We attribute the difference at $t = 6 \text{ s}$ to shear induced crystallization that we neglected in the calculation. It is known that application of shear will substantially increase the number of nucleating centers, thereby increasing the rate of crystallinity (23,24). This effect will be confined to the region near the skin, which experiences shear flow during the initial mold fill. It is possible to simulate shear induced crystallization in the model calculation by increasing the number of nucleation centers at short times. When this was done, closer agreement with the observed data was achieved.

In Fig. 15 we show calculated light intensities for maximum $\chi = 0.47, 0.50,$ and 0.53 holding the mold temperature constant at 38°C . The lower the crystallinity, the sooner crystallization is complete and the higher is the final plateau of light intensity. If we carry out the calculations at different mold temperatures in accordance with the data of Fig. 7, we obtain curves similar to those of Fig. 15. Thus, the sensor could be calibrated to measure crystallinity of the molded polypropylene product.

SUMMARY

An optical sensor, which consists of optical fibers inserted into a sleeved ejector pin with a sapphire window at its end, was used to monitor the injection molding of polypropylene. In our experiments, light from a helium neon laser was transmitted via the optical sensor to the mold cavity where it traversed the thickness of the resin, reflected from the back wall of the mold, retraced its path through the resin and was collected by the sensor optical fibers. Scattering due to the growing microcrystals resulted in attenuation of the light and produced characteristic quadratic scattering due to the spherulitic morphology of crystallization. A model was developed from which light transmission was calculated as a function of the crystallization and time. The model describes effects on the transmitted light due to crystallization kinetics and illustrates the role of temperature and pressure during the crystallization. In particular, the model illustrates how applied pressure increases the crystallization rate by increasing resin supercooling and produces compression heating and cooling upon application and release of pressure. Also, the model describes the special circumstances under which core crystallization takes place, namely at atmospheric pressure causing relatively slow crystallization accompanied by a substantial increase in temperature.

APPENDIX

The calculations of temperature and crystallinity arrays (Figs. 11–13) were carried out using established techniques for finite element difference calculations (25). The resin thickness was divided into 82 elements and the steel mold (2.54 cm thickness) was divided into 10 elements. A thermal resistance was positioned at the resin/steel interface. The boundary conditions are: insulating boundaries at the resin core and at the outside of the steel mold, at the resin core $dT/dx = 0$, and the heat flux across the resin/mold interface is continuous. The temperature functions at the boundaries were evaluated using a second order Taylor series forward difference equation (25). The values of C_p and k as a function of temperature were placed in a look-up table and evaluated at the element temperature using an interpolation procedure. The value of dk/dx was obtained from the product $(dk/dT)(dT/dx)$, where dT/dx was calculated from the difference in temperature between neighboring elements and dk/dT

was obtained from literature values stored in the look-up table. Starting with initial conditions of resin and mold temperatures at 220°C and 38°C , the initial temperature changes were evaluated using Eq 2 by explicitly calculating the heat flux transport at each element of resin and steel during the established time increment, 1 ms. The process begins with heat transport into the steel mold from the resin element at the resin/steel interface. The resultant temperature drop sets in motion a process of heat transport through all resin elements in the next time increment. If compression heating and/or crystallization do not occur, the calculation yields uniformly decreasing temperature arrays. Crystallization and compression heating add a layer of complication because competing heat quantities can either raise or lower both the local temperature and the rate of crystallization. At each time step, the crystallinity and temperature were updated and used as the basis for calculations during the next time step. For example, dT/dt was obtained from the difference between the current temperature and the old temperature divided by the time step, and crystallinity in element i was calculated from $\chi(i) = \chi(i)_{old} + \dot{\chi}(i)dt$, where $\dot{\chi}(i)$ was calculated from the Avrami equation. Crystallization is irreversible; once crystallized an element was not permitted to remelt even though its temperature subsequently increased. Such local temperature increases were found to be less than 8°C except at the core where larger temperature increases occurred.

Non-linear effects due to crystallization have the potential of launching the calculation into an unstable condition. We have avoided instabilities by using two devices. First, the Fourier coefficient F_0 , calculated for each element, is maintained at a value less than 0.5. Here,

$$F_0 = \frac{k(i)dt}{\rho C_p(i) dx^2}$$

where $k(i)$ and $C_p(i)$ are thermal conductivity and heat capacity at element i , ρ is density, dt is the time increment, and dx is the element thickness (25). By judicious choice of dt and dx , we can achieve $F_0 < 0.5$ for all times. Second, the maximum temperature change in any element during the time step is not permitted to be greater than 1°C . Should the potential change in temperature during the time step dt be larger than 1°C , then the time increment is subdivided into smaller steps so that ΔT always remained less than 1°C for any time step. While 1 ms was the nominal time step employed for the calculation, there were instances for which the temperature change dictated smaller time increments.

REFERENCES

1. A. J. Bur, F. W. Wang, C. L. Thomas, and J. L. Rose, *Polym. Eng. Sci.*, **34**, 671 (1994).
2. A. J. Bur and C. L. Thomas, *Polym. Eng. Sci.*, **37**, 1430 (1997).

3. A. J. Bur and C. L. Thomas, *Proc. SPE ANTEC*, **40**, 490 (1994).
4. A. J. Bur and C. L. Thomas, *Proc. SPE ANTEC*, **41**, 2798 (1995).
5. A. J. Bur and C. L. Thomas, *Proc. SPE ANTEC*, **42**, 627 (1996).
6. Identification of a commercial product is made only to facilitate experimental reproducibility and to describe adequately experimental procedure. In no case does it imply endorsement by NIST or imply that it is the best product for the experiment.
7. C. L. Thomas, A. A. Tseng, A. J. Bur, and J. L. Rose, *Adv. Polym. Tech.*, **15**, 151 (1996).
8. C. L. Thomas, A. O. Adebo and A. J. Bur, *Proc. SPE ANTEC*, **40**, 2236 (1994).
9. M. Jeng, C. L. Thomas, R. Peterson and A. J. Bur, *Proc. Soc. Mech. Eng., Dallas Mtg.*, Nov. 1997.
10. J. P. Runt, in *Encyclopedia of Polymer Science and Engineering*, Vol. 4, p. 482, H. F. Mark, N. M. Bikales, C. G. Overberger, and G. Menges, editors, John Wiley, New York (1986).
11. M. B. Rhodes and R. S. Stein, *J. Polym. Sci.*, **45**, 521 (1960).
12. D. Y. Yoon and R. S. Stein, *J. Polym. Sci. Polym. Phys.*, **12**, 735 (1974).
13. D. W. Van Krevelen, *Properties of Polymers*, Elsevier, New York 1990.
14. B. Wunderlich, *Macromolecular Physics*, Vol. 1 and 3, Academic Press, New York (1980).
15. M. Kamal, A. Mutel, G. Salloum and A. Garcia-Rejon, *Proc. SPE ANTEC*, **37**, 483 (1991).
16. H. B. Callen, *Thermodynamics*, John Wiley, New York (1960).
17. B. Hartmann and M. A. Haque, *J. Appl. Polym. Sci.*, **30**, 1553 (1985).
18. P. Zoller, *J. Appl. Polym. Sci.*, **23**, 1057 (1979).
19. C. A. Hieber, *Polymer*, **36**, 1455 (1995).
20. L. Mandelkern, N. L. Jain, and H. Kim, *J. Polym. Sci. Pt. A-2*, **6**, 165 (1968).
21. E. Martuscelli, M. Pracella, M. Avella, R. Greco, and G. Ragosta, *Makromol. Chemie*, **181**, 957 (1980).
22. U. Leute, W. Dollhopf, and E. Lisha, *Colloid Polym. Sci.* **256**, 914 (1978).
23. M. D. Wolkowicz, *J. Polym. Sci. Polym. Symp.*, **63**, 365 (1978).
24. A. I. Isayev, T. W. Chan, K. Shimojo, and M. Gmerek, *J. Appl. Polym. Sci.*, **55**, 807 (1995); also, *J. Appl. Polym. Sci.*, **55**, 821 (1995).
25. C. Tucker, *Fundamentals of Computer Modeling for Polymer Processing*, Hanser Publishers, New York, (1989).